

Geochemistry, Geophysics, Geosystems®

RESEARCH ARTICLE

10.1029/2021GC010149

Key Points:

- Site responses at central CA are strongly affected by surface lithology and consolidation degree of sediments, rather than their thickness
- Lg Q values are low compared to other regions in US, reflecting tectonic activity, presence of fluid and/or soft lithology in the region
- Site response correction on the two-station method enhances depth sensitivity of Lg Q estimates by suppressing surficial effects

Supporting Information:

Supporting Information may be found in the online version of this article.

Correspondence to:

Y. Kim,
younghkim@snu.ac.kr

Citation:

Yun, J., Kim, Y., & Clayton, R. W. (2022). Spatial variation and frequency dependence of Lg wave attenuation with site response correction along the CCSE array in Central California, US. *Geochemistry, Geophysics, Geosystems*, 23, e2021GC010149. <https://doi.org/10.1029/2021GC010149>

Received 7 SEP 2021
Accepted 27 DEC 2021

Author Contributions:

Conceptualization: YoungHee Kim
Data curation: Jeena Yun, Robert W. Clayton
Formal analysis: Jeena Yun, YoungHee Kim
Funding acquisition: YoungHee Kim
Investigation: Jeena Yun, YoungHee Kim
Methodology: Jeena Yun, YoungHee Kim
Project Administration: YoungHee Kim
Resources: YoungHee Kim

© 2022. The Authors.

This is an open access article under the terms of the Creative Commons Attribution-NonCommercial-NoDerivs License, which permits use and distribution in any medium, provided the original work is properly cited, the use is non-commercial and no modifications or adaptations are made.

Spatial Variation and Frequency Dependence of Lg Wave Attenuation With Site Response Correction Along the CCSE Array in Central California, US

Jeena Yun¹ , YoungHee Kim¹ , and Robert W. Clayton² 

¹School of Earth and Environmental Sciences, Seoul National University, Seoul, Republic of Korea, ²Seismology Laboratory, Division of Geological and Planetary Sciences, California Institute of Technology, Pasadena, CA, USA

Abstract We estimate lateral Lg wave attenuation (Q) structure at four center frequencies (0.75, 1, 2 and 2.75 Hz) along the Central California Seismic Experiment array in western US crossing the San Andreas Fault and Central Valley. We take two steps in constructing the site-response-corrected Lg Q model: (a) we compute relative site responses at each station using the reverse two-station method, and (b) we estimate Q values based on the two-station method after removing the site term. Removal of the site response in the Q model allows to probe laterally varying Q properties at mid-to-lower crustal depths. Our model follows a power-law frequency dependence as $Q(f) = (81 \pm 8)f^{(0.62 \pm 0.11)}$, reflecting the active tectonic setting and the presence of fluids in the region. A change in lithology from softer sediments near Pacific coast to harder basements near Sierra Nevada correlates well with the increasing trend of the Lg Q values towards east. Our laterally varying estimates at lower frequencies generally follow the variation of shear-wave velocities at deeper crustal depth and Moho temperature, whereas those at higher frequencies mostly follow the shear-wave velocity variation at shallow depth. Positive site responses obtained by reverse two-station method are found at 34 stations out of total 46 stations examined, and their responses are mostly correlated with surficial lithology (i.e., sedimentary rocks) along the profile, rather than the thickness of the sediments. The site responses also exhibit a strong negative correlation to the V_{S30} data.

1. Introduction

Lg wave is well known as the most prominent phase in high frequency seismograms that travels through a continental path. The Lg is often modeled either as a sum of higher mode surface waves (Knopoff et al., 1973; Oliver et al., 1957) or as a superposition of critically reflected S waves (Bouchon, 1982). Kennett (1986) reported that the Lg wave dissipates significantly into other phases such as Sn as the crust gets thinner, implying that the Lg wave can only propagate on the continental path. This restriction in pathway makes it powerful for imaging continental seismic structures since there is little chance of oceanic contamination. In the virtue of its uniqueness, the Lg is utilized in diverse field of seismic investigations such as magnitude measurement (m_b [Lg]; Nuttli, 1973; Zhao et al., 2008) or discrimination between natural earthquakes and manmade explosions at regional distances (Blandford, 1981). Mapping crustal heterogeneities with Lg wave attenuation has also been one of the major applications, conducted by a number of studies in various regions (e.g., Hasegawa, 1985-Canadian shield; Xie & Mitchell, 1990a-continental Africa; Baqer & Mitchell, 1998-continental United States; Xie et al., 2004-Tibet; Ranasinghe et al., 2015-northeast China; Noriega et al., 2015-Iberian Peninsula; He et al., 2017-eastern Mongolia; Wei et al., 2017-Australia).

Lg wave is highly useful for constraining the quality factor Q , because it can be easily identified even for small-magnitude events owing to its large amplitude, and is almost always present in the seismogram of continental path. Lg Q is often assumed to obey a power-law frequency:

$$Q(f) = Q_0 f^\eta \quad (1)$$

where Q_0 is the Q value at 1 Hz and η is the frequency dependence factor. Both Lg Q_0 and η tend to have a strong correlation with the tectonic activity of a region: low Q_0 and high η values in tectonically active regions whereas high Q_0 and low η values in stable regions (Benz et al., 1997; Erikson et al., 2004; Singh & Herrmann, 1983). Lg Q_0 is also highly sensitive to the temperature and presence of fluids in the crust (Frankel, 1991; Mitchell, 1995;

Software: Jeena Yun
Supervision: YoungHee Kim
Validation: Jeena Yun, YoungHee Kim, Robert W. Clayton
Visualization: Jeena Yun
Writing – original draft: Jeena Yun
Writing – review & editing: Jeena Yun, YoungHee Kim, Robert W. Clayton

Mitchell et al., 1997). These properties make $Lg Q$ more useful when examining regional variation of the crustal structure and provide key constraints on material properties and structure.

Among several methods that are available for estimating the $Lg Q$, two-station method (TSM), initially suggested by Tsai and Aki (1969), is widely used since it can suppress site and source effects by using spectral ratio of a two-station pair. Reverse two-station method (RTSM) provides even better accuracy than the TSM, since the site terms are eliminated almost perfectly by using two events simultaneously recorded at two stations. Ford et al. (2008) compared five methods used for the estimation of the one-dimensional variation of $Lg Q$, and showed that TSM has low dependence on parameter selection except for the choice of the frequency band. RTSM was nearly undisturbed by parameter selection, but the strict geometry requirement of the method greatly reduces the quantity of available data set (Ford et al., 2008). Therefore, we adopt the TSM for the investigation of $Lg Q$ and use RTSM only for the estimation of relative site responses.

Several studies on the Lg wave attenuation structure of the United States have been conducted with various methodologies (Table S1 in Supporting Information S1). Singh and Herrmann (1983) estimated Lg coda Q at 1 Hz and η for the entire US, using a scattering model. They reported low Q_0 values of 140–200 for western US which gradually increase toward northeast direction, reaching 700–900 in north-eastern US. Baquer and Mitchell (1998) used stacked spectral ratio method to provide a tomographic map of Lg coda Q_0 and the η for the contiguous US, presenting lower Q values (<500) west to the Rocky Mountain and higher Q values (>500) east to the mountain. Particularly, they observed the lowest Q_0 value of 250–300 in the Pacific coastal regions. More recently, Phillips and Stead (2008) provided a high-resolution two-dimensional tomographic map of $Lg Q_0$ for western US, showing Q values within 80–200 in Central California. They associated high Q values with stable cratons or intrusive igneous batholiths (e.g., Colorado and Columbia Plateaus, Sierra Nevada) and low Q values with tectonically active regions (e.g., coastal California, Yellowstone). Gallegos et al. (2014) performed both TSM and RTSM to obtain tomographic map of $Lg Q_0$ for central and eastern US. Both methods showed generally similar pattern of $Lg Q_0$ values, ranging from 200 to 1,600. Gallegos et al. (2014) highlighted a linkage between the level of Lg wave attenuation and heat flow, sediment thickness, age of the geologic terrane, and their composition. Mitchell et al. (2015) performed a continent-wide tomography of Lg coda Q at 1 Hz using the stacked spectral ratio method. Lg coda Q_0 values are predominantly low (200–350) along the western coast and gradually increased toward east, being the highest (700–1,000) at the Canadian Shield. Gallegos et al. (2017) adopted the TSM at four different frequencies (0.5, 1, 2 and 3 Hz) to conduct $Lg Q$ tomography in western US. At 1 Hz, $Lg Q$ values of 80–250 are obtained in Central California, and the values tend to increase as the center frequency increases.

Site response has also been investigated actively, and many of them exploited the RTSM for the estimation. For example, Gallegos et al. (2017) provided maps of relative site responses in western US, centering at 0.5, 1, 2 and 3 Hz. De-amplification is observed at hard rock regions (e.g., Sierra Nevada, Snake River Plain) whereas amplification is dominant at softer sedimentary regions (e.g., Basin and Range). However, they did not interpret the westernmost part of the US due to the low resolution. In central-eastern US, Yassmin et al. (2019) estimated relative site responses with four center frequencies (1, 2, 3 and 4 Hz). They reported a strong correlation of the site responses to the basins and sediments, the topography of the region and the surface shear-wave velocity (i.e., V_{S30}).

Despite the large number of previous studies, there is only scarce or no detailed reports on both $Lg Q$ and site response in westernmost end of the US. This is because the region frequently lacks the resolution, lying within the edge of inversion grids in large-scale studies. Considering its complex crustal setting and seismic hazard assessment, it is important to provide estimates on both $Lg Q$ and site response in westernmost US.

In this study, we investigate lateral variation and frequency dependence of crustal $Lg Q$ along a great circle profile in westernmost part of the US, using the dense seismic array data acquired from Central California Seismic Experiment (CCSE; Jiang et al., 2018). To take full advantage of the dense linear array, we focus on one-dimensional lateral variation of $Lg Q$ beneath the array with the highest resolution using the TSM and RTSM rather than two-dimensional tomography approach. Investigation of the lateral $Lg Q$ variations along the array is invaluable in that it crosses several geologically important features such as a major plate-boundary fault (i.e., the San Andreas Fault), thick sedimentary basin (i.e., the Central Valley) and massive mountain ranges (i.e., Sierra Nevada). Moreover, basements beneath the CCSE array also vary from metasedimentary Franciscan Complex (Bennington et al., 2008) to igneous Sierra Nevada batholith (Godfrey & Klemperer, 1998). Along with the Q structure, we

obtain relative site responses at each station to consider the effect of site amplification, and use the estimates to correct the $Lg Q$ structure. Based on this study, we aim to provide deeper insight into the nature of $Lg Q$ attenuation with the known geologic features and also in the considered frequency range.

2. Geologic Setting

The CCSE array extends from the Pacific coast to the Sierra Nevada foothills in east-west direction, crossing several geologically unique features: the creeping section of the San Andreas Fault (SAF) and 100-km wide Central Valley (CV) forearc basin (Figure 1). The SAF is a long, right-lateral strike-slip fault system traversing the western coast of the US. Although direct causal relationship between the SAF and the $Lg Q$ has not been established yet, the SAF can affect the Q value as it can provide a channel for fluid migration. Moreover, several lines of geophysical evidence such as a sharp contrast of P -wave velocity structure (Eberhart-Phillips & Michael, 1993) illustrate that the fault zone can act as a boundary of two distinct basements. The CV is a massive forearc basin, which is formed during the Mesozoic subduction of the Pacific Plate underneath the North American Plate. The basin is mainly filled with Quaternary alluvium and marine sediments (Jennings et al., 1977), most of which is unconsolidated or loosely consolidated (Farrar & Bertoldi, 1988; Poland & Evenson, 1966). Generally, unconsolidated sedimentary layers are known to cause strong attenuation of the Lg wave, which leads to low $Lg Q$ values (Hong, 2010; Mitchell & Hwang, 1987; Wei et al., 2017; Zhao & Mousavi, 2018; Zhao et al., 2010).

The deeper lithology beneath the CCSE array changes abruptly, transitioning from harder Salinian block into softer metasedimentary Franciscan complex (Page, 1981). The Salinian block is an aggregate of Cenozoic granitic and metamorphic rocks, which has been transported northwestward by the right-lateral movement of the SAF. The block exhibits high resistivity (Becken et al., 2008; Unsworth & Bedrosian, 2004), high seismic velocity (Eberhart-Phillips & Michael, 1993; Zhang & Thurber, 2005), and high P - and S -wave attenuation (Q_p and Q_s , respectively; Bennington et al., 2008; Eberhart-Phillips, 2016). The Franciscan complex is an accretionary wedge that is formed during the Mesozoic subduction. The effect of the Franciscan complex to the attenuation still remains unclear: Bennington et al. (2008) speculated that the high Q values imaged by the body-wave attenuation tomography might be the result of the closure of cracks in the rocks of the complex, whereas Eberhart-Phillips (2016) reported moderately low Q value for the Franciscan complex from the P - and S -wave attenuation models.

Farther toward inland, a 10–12 km thick Great Valley Ophiolite (GVO) underlies the CV which is a mafic oceanic crust that has been obducted onto the continental crust during Jurassic Nevadan orogeny (Godfrey & Klemperer, 1998; Godfrey et al., 1997). The GVO is imaged as high Q by body-wave attenuation tomography

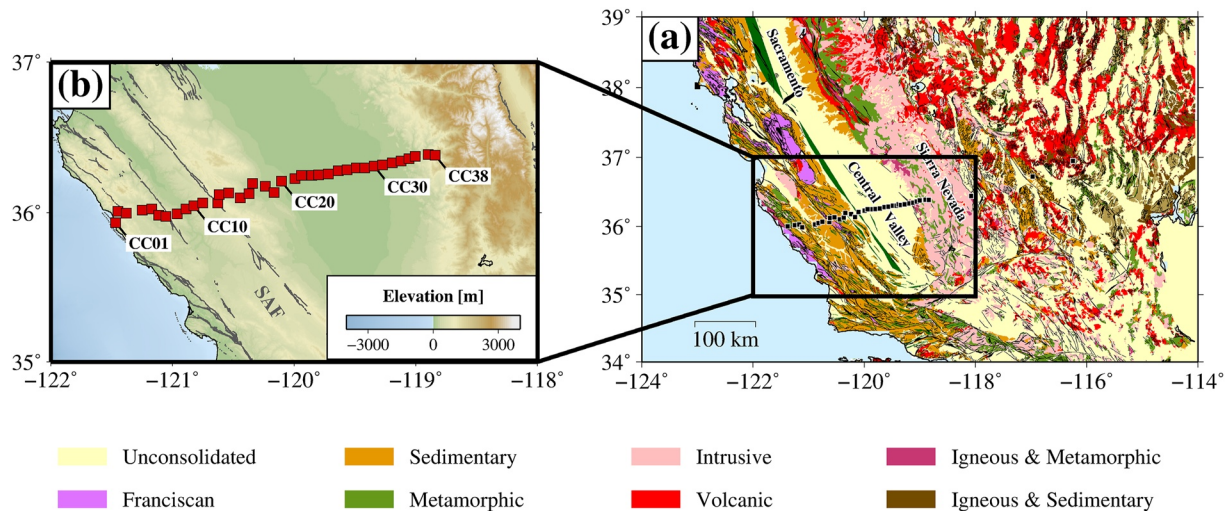


Figure 1. Geological map showing the CCSE array in Central California, US. (a) Simplified geological map of Central California (Jennings et al., 1977; USGS) and (b) distribution of the CCSE array. Black box in panel (a) indicates the location of panel (b). Rock types and associated color legends are shown below the panels (a) and (b). (SAF: San Andreas Fault).

(Eberhart-Phillips, 2016; Eberhart-Phillips et al., 2014). At the easternmost part of our study region, there lies an old and stiff Sierran Basement, which is mainly consisted of Mesozoic granitic rocks (Godfrey & Klemperer, 1998). High Q values are reported for the Sierran Basement from analyses of body wave (Eberhart-Phillips, 2016) and Lg wave (Gallegos et al., 2017; Phillips & Stead, 2008).

In addition to complex crustal lithology, an anomalous seismic feature beneath the CV is detected as high velocities at upper mantle depth (>40 km), called the Isabella anomaly. Two main hypotheses are put forward as its tectonic origin: the anomaly is interpreted as either a remnant fossil slab fragment (Dougherty et al., 2021; Jiang et al., 2018; Pikser et al., 2012; Wang et al., 2013) or a founded lithosphere that was detached from the Sierran Basement (Boyd et al., 2004; Zandt et al., 2004). The Isabella anomaly can affect the composition of the lowermost crust and its origin can be highly relevant with local crustal evolution.

3. Data Processing

We used 637 crustal earthquakes that occurred during January 2013–December 2016 recorded by the CCSE array, Southern California Seismic Network (CI) and Southern Great Basin Network (SN) stations (Figure 2). CI and SN stations located farther east to the CCSE array are selected to improve the spatial coverage. Among the CCSE stations, we exclude data from station CC36 because they showed anomalously low amplitudes compared

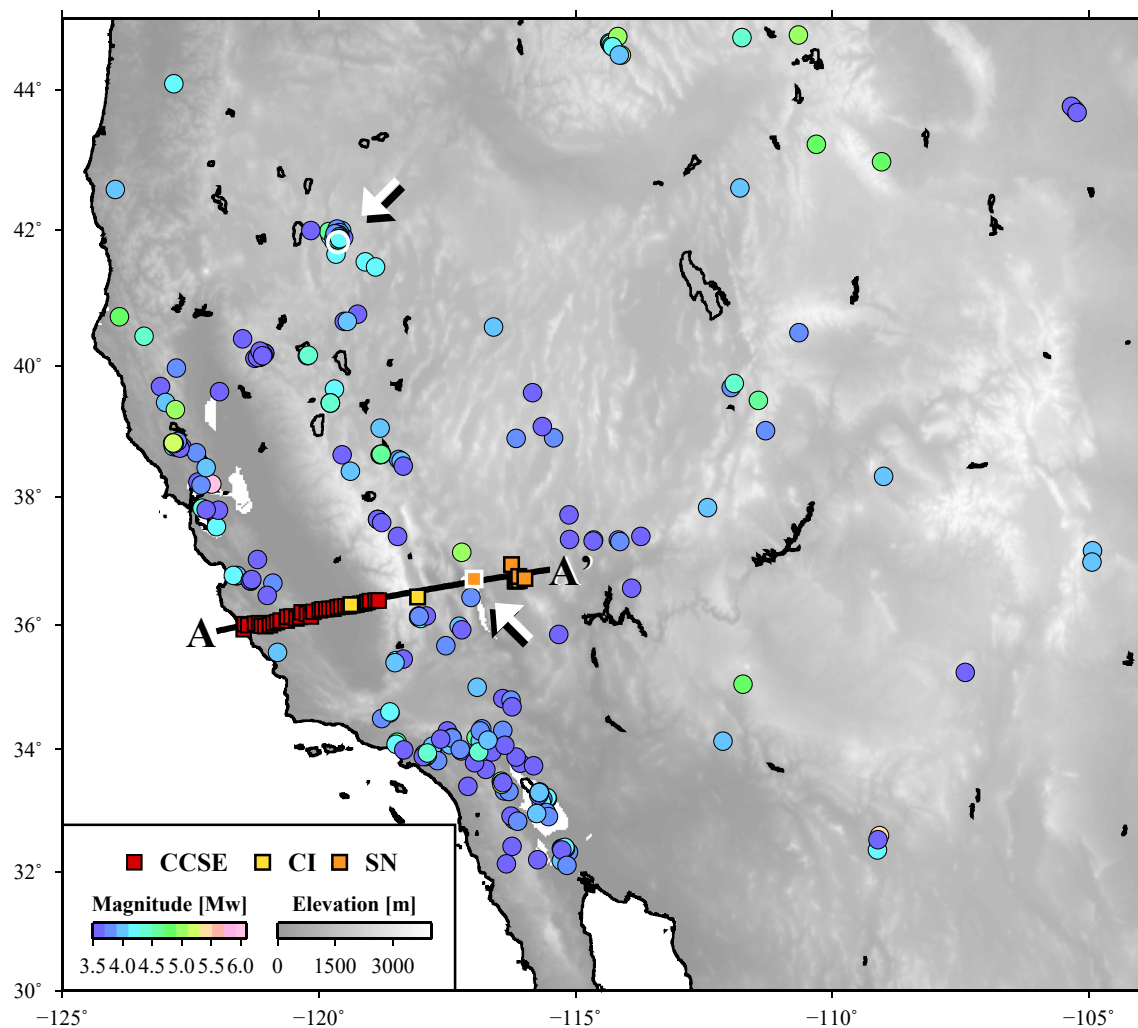


Figure 2. Location of earthquakes (circles) and stations (squares) used in this study. Red squares represent the CCSE array stations, yellow squares represent the Southern California Seismic Network (CI) and orange squares represent the Southern Great Basin Network (SN). The event and station bounded by the white line and marked with the white arrow (event 150727_M4.4 and station HEL) are referred in the example shown in Figure S4 in Supporting Information S1.

to those from the nearby stations (i.e., CC35 and CC37). We used data from the stations that recorded more than three events.

The moment magnitude of the events ranges from 3.5 to 6.1. Events are filtered primarily according to their location, only keeping those events that have little or no chance of traveling oceanic paths. It is well known that the Lg phase is hard to distinguish from the Sg phase at local distances (≤ 200 km; Kennett, 1983; Xie & Mitchell, 1990b) or even becomes incoherent at teleseismic distances ($> 2,000$ km; Gallegos et al., 2017). In order to ensure the generation of Lg wave, we strictly retained seismic records with regional epicentral distance, between 250 km and 2,000 km. After the screening, total 531 events are left, recorded at 37 CCSE array stations (CC01–CC38; except CC36), two CI stations and seven SN stations (Table S2 in Supporting Information S1). We bandpass filtered vertical component of the remaining seismograms with bandwidths of 0.375–1.125 Hz, 0.5–1.5 Hz, 1.0–3.0 Hz, and 1.375–4.125 Hz, centering at 0.75, 1, 2, and 2.75 Hz, respectively. The center frequencies and their bandwidths are determined following the approaches of Gallegos et al. (2017) and Ranasinghe et al. (2018) and also considering factors such as signal-to-noise ratio, ray-paths and resolution for the inversion (Figure S1 in Supporting Information S1). The mean, trend and instrumental responses are then removed (Figure S2 in Supporting Information S1).

The quality of data is controlled based on the signal-to-noise ratio (SNR). We screened the data twice, first using the root mean square (RMS) amplitude in time domain and then using the Fourier transformed spectra in frequency domain. To measure the SNR, we set Lg window and noise window in each seismogram. The window for Lg wave is automatically determined based on the group velocity, to begin at 3.6 kms^{-1} and terminate at 3.0 kms^{-1} (i.e., Gallegos et al., 2017; Phillips & Stead, 2008; Zhao, Xie, Wang, et al., 2013). The noise window is defined to have the same length in time domain with the Lg window and to end at the theoretical arrival time of P wave. 10% buffer is appended to either side of both windows to allow minor fluctuation in actual wave arrival.

Using the data within each window, we calculated SNR of the RMS amplitude of each seismogram, and excluded the records if the SNR is less than 2 (Figure S3 in Supporting Information S1). For those records that passed the RMS SNR criteria, both Lg and noise windows are transformed into the frequency domain via Fast Fourier Transformation (FFT), with 20% cosine taper window (Figure S4b in Supporting Information S1). Following the procedure by Zhao et al. (2010), we used spectral amplitudes on 58 reference frequencies that are distributed log-evenly from 0.05 to 10.0 Hz. Power spectral amplitudes at each point are estimated differently at lower (≤ 0.5 Hz) and higher (≥ 0.5 Hz) frequencies. For lower frequencies, we used the Lagrangian interpolation after 3-point running average smoothing (Xie & Mitchell, 1990b), while the RMS method suggested by Zhao et al. (2010) is adopted for higher frequencies. Assuming that raw Lg spectra contain both pure Lg and noise component and the two are independent of each other, spectral amplitude of the pure Lg wave can be estimated using the relationship: $A_{\text{pure}}^2(f) = A_{\text{raw}}^2(f) - A_{\text{noise}}^2(f)$ where A denotes the amplitude in frequency domain (Figure S4b in Supporting Information S1; Zhao et al., 2010). We took the ratio of the spectral amplitudes of the pure Lg and noise (i.e., $A_{\text{pure}}/A_{\text{noise}}$) for every 58 points, and selectively kept the point only when the ratio is greater than 2 (Figure S4c in Supporting Information S1). After the quality control, about 272–322 events are left depending on the center frequencies and the maximum epicentral distance reduced into $\sim 1,620$ km.

4. Methods

To investigate lateral variations of $Lg Q$ along a great circle profile (A–A'; Figure 2), we first chose two-station pairs that satisfy azimuthal and back-azimuthal difference criteria ($\delta\theta < 15^\circ$). For all possible two-station pairs, interstation $Lg Q$ values are measured using the TSM. We then divided the profile into several cells, assuming that the Q value inside each cell is uniform. Finally, we inverted the interstation $Lg Q$ values into the Q values in each cell, using the Levenberg–Marquardt method (Levenberg, 1944; Marquardt, 1963). In addition, relative site responses at each station are estimated by the RTSM. Details for each step are described in the subsequent sub-sections.

4.1. Two-Station Method (TSM)

In general, the spectral amplitude $A(f, \Delta)$ recorded on a station can be represented as below:

$$A(f, \Delta) = S(f)I(f)E(f)G(\Delta)\exp\left(\frac{-\pi f \Delta}{v_{Lg}Q(f)}\right) \quad (2)$$

where f refers to the frequency, Δ refers to the epicentral distance, v_{Lg} refers to the Lg wave group velocity (3.5 km s^{-1} in this study), S refers to the source spectrum, I refers to the instrumental response at the station, E refers to the site response, and Q refers to the frequency-dependent quality factor. In this study, we remove the instrumental response I during the data processing stage. The geometrical spreading $G(\Delta)$ can be expressed with a constant G_0 and geometrical spreading coefficient m as follows:

$$G(\Delta) = G_0 \Delta^{-m}. \quad (3)$$

Since we only use epicentral distances larger than 250 km, it is valid to assume $m = 0.5$ (Yang, 2002). By taking ratio of spectral amplitudes from two stations (stations 1 and 2) recording the same event (event a), source spectra S can be eliminated provided that the two stations have nearly identical azimuths. Then, we can estimate interstation Q value using the spectral ratio:

$$\frac{v_{Lg}}{\pi \Delta_{12}} \ln \left[\frac{E_2 A_{1a} \Delta_{1a}^{1/2}}{E_1 A_{2a} \Delta_{2a}^{1/2}} \right] = \frac{f}{Q(f)} \quad (4)$$

where interstation distance $\Delta_{12} = \Delta_{2a} - \Delta_{1a}$. In conventional TSM, the ratio of E_1 to E_2 is regarded as unity. However, we assess the validity of the assumption of uniform site responses since geologic properties along the great circle profile in our study region vary rapidly in a relatively short distance range. We therefore correct for the site response term by substituting E_1 and E_2 values with the estimates from the RTSM, and compare the result with that from the conventional TSM.

When constructing the two-station pairs, azimuthal difference between the two stations ($\delta\theta$) is often non-zero (Figure 3b). Deviation from the perfect linear geometry gives rise to potential errors in Q estimates since non-isotropic source radiation can affect the result and far-field information might also be included. To minimize such errors, we constrained both azimuthal and back-azimuthal deviation to be less than 15° (Der et al., 1984; Gallegos et al., 2017). For all possible two-station pairs that passed the criteria, interstation Lg Q values are measured by fitting discrete left-hand side values of Equation 4 into a curve. To screen out extreme Q values, we only used Q estimates between the range of 10–2,000, and excluded the estimates if they were larger than 1.5 times the standard deviation. Also, we considered the relative error in interstation Q values, which can be estimated as follows (Xie et al., 2004):

$$\frac{\delta Q}{Q} = \frac{v_{Lg}}{f\pi} \left(\frac{Q}{\Delta_{12}} \right) \delta x \quad (5)$$

where δQ is the error in interstation Q measurement and δx is a small term expressing the level of modeling error, assumed to have a value of 0.2 in this study. We regulated Δ_{12} to be larger than 30 km to ensure low level of relative error, and discarded the pairs when its relative error ($\delta Q/Q$) is greater than 0.4. Final ray coverages that satisfy all these criteria are shown in Figure S5 in Supporting Information S1.

To invert the interstation Q values into the laterally varying Q values, we segmented the great circle profile into several cells. Assuming that Q value is uniform within the cell, we can estimate the representative Q value for the m -th cell (i.e., Q_m ; $m = 1, 2, \dots, M$) through following linear relationship:

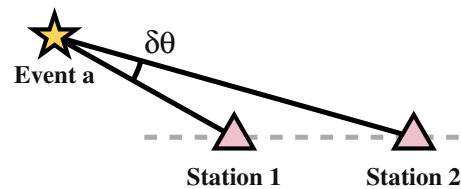
$$\frac{\Delta_n}{Q_n} = \sum_{m=1}^M \frac{\Delta_{mn}}{Q_m} \quad (6)$$

where Δ_n is an interstation distance for the n -th ray ($n = 1, 2, \dots, N$), Q_n is the interstation Q value for the n -th ray, and Δ_{mn} is the length of the n -th ray passing through the m -th cell. Equation 6 can then be represented by a linear system $\mathbf{d} = \mathbf{Gm}$, where \mathbf{d} is a vector consisting of the left-hand side of Equation 6, \mathbf{G} is a matrix composed by Δ_{mn} values and \mathbf{m} being a vector having values of $1/Q_m$. The system can be solved iteratively under the least squares scheme using the Levenberg-Marquardt method (Gavin, 2019; Levenberg, 1944; Marquardt, 1963; MATLAB code from). To prevent extreme values, we imposed following mild smoothing during each step of the iteration:

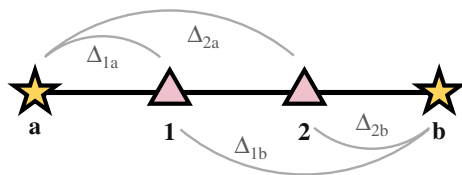
(a) Ideal TSM



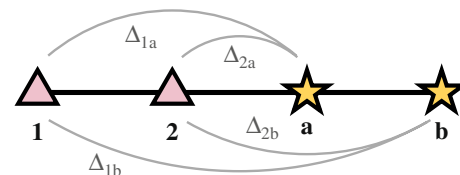
(b) Realistic TSM



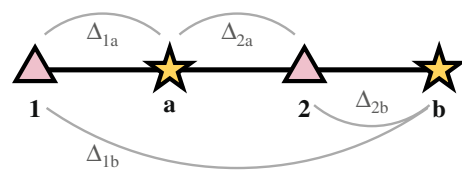
(c) RTSM



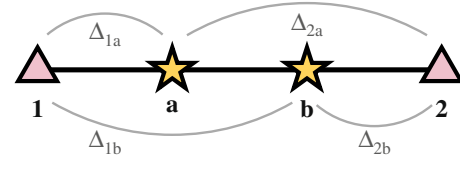
Case 1



Case 2



Case 3



Case 4

△ : Station ★ : Event

Figure 3. Event-station geometries for two-station method (TSM) and reverse two-station method (RTSM). (a) An ideal geometry for the TSM, and (b) more realistic geometry for the TSM. The azimuthal difference and back azimuthal difference ($\delta\theta$) are regulated to be smaller than 15° for both TSM and RTSM. (c) Four possible station-event geometries for the RTSM. Case 1 represents a geometry when both events are outside the two stations and at either side of the station. Case 2 assumes when both events are outside the two stations, but at the same side of the stations. Case 3 describes a situation when one event sits between the two-station pairs while the other is outside of the pairs. Case 4, also known as the RTEM geometry, represents a geometry when both events lie within the two-station pair.

$$\text{new}Q_m = \frac{1}{12}[Q_{m-1} + 10Q_m + Q_{m+1}]. \quad (7)$$

In this study, we exploited the events that are located north and south of the linear array to compensate the deficiency of the events west to the array. Since conventional TSM requires events that align almost linearly to the station array, we further explored the effect of station-event geometry on the final Q estimates. At 1 Hz, two-station pairs were divided into two groups, “linear” and “off-linear”, and we compared the distribution of Q_0 values for each group. For the classification, we computed the angle between a line that connects the two stations and another line that connects an event to one of the stations. Two angles were then obtained for a single two-station pair, and we classified the pair as “linear” only when the larger angle among the two is less or equal to 15° . As a result, we did not observe systematic bias according to the station-event geometry (Figure S6 in Supporting Information S1). This consistency also holds for other center frequencies (0.75, 2, and 2.75 Hz).

4.2. Reverse Two-Station Method (RTSM)

Relative site responses at each station are estimated using the RTSM. Unlike the TSM, the RTSM utilizes a pair of two stations (stations 1 and 2) and two events (events a and b) lying almost linearly (Figure 3c). By multiplying the spectral ratios from the two station-event pairs, following relationship can be achieved (Bao et al., 2011; Gallegos et al., 2017):

$$\ln(E_1) - \ln(E_2) = \frac{\Delta_{1b} - \Delta_{2b}}{\Delta_{2a} - \Delta_{1a} - \Delta_{2b} + \Delta_{1b}} \ln\left(\frac{A_{1a}\Delta_{1a}^m}{A_{2a}\Delta_{2a}^m}\right) + \frac{\Delta_{2a} - \Delta_{1a}}{\Delta_{2a} - \Delta_{1a} - \Delta_{2b} + \Delta_{1b}} \ln\left(\frac{A_{1b}\Delta_{1b}^m}{A_{2b}\Delta_{2b}^m}\right). \quad (8)$$

A physical meaning of the denominator of the coefficients in the right-hand side of above equation (i.e., $\Delta_{2a} - \Delta_{1a} - \Delta_{2b} + \Delta_{1b}$) is the difference in the interstation distance from event a and b (Chun et al., 1987). When constructing the RTSM pairs, we excluded the pairs that lack the physical meaning (cases 3 and 4 in Figure 3c). The relationship between the interstation distances from event a (i.e., $\Delta_{1a} - \Delta_{2a}$) and that from event b (i.e., $\Delta_{1b} - \Delta_{2b}$) also plays a critical role in screening the RTSM pairs, particularly if their magnitudes are approximately identical. If they have the same sign (case 2 in Figure 3c), the right-hand side might have an unexpectedly large value since the denominator becomes very small. Otherwise (case 1 in Figure 3c), the coefficients would approximate 0.5, greatly stabilizing the estimation. Hence, along with the linearity criterion (i.e., $\delta\theta < 15^\circ$), we strictly used the case 1 geometry.

Equation 8 can be represented by a linear system $\mathbf{f} = \mathbf{Hk}$, where vector \mathbf{f} corresponds to the right-hand side values of Equation 8 and vector \mathbf{k} represents the desired log site responses. A sparse matrix \mathbf{H} represents the coefficients of the two log terms in the left-hand side of Equation 8:

$$\mathbf{H} = \begin{bmatrix} 1 & -1 & 0 & 0 & 0 \\ 1 & 0 & -1 & \cdots & 0 & 0 \\ 0 & 1 & -1 & 0 & 0 \\ \vdots & & \ddots & & \vdots \\ 0 & 0 & 0 & \cdots & 1 & -1 \end{bmatrix}. \quad (9)$$

Since the RTSM only provides the difference between the stations, we can only estimate the site responses relative to several reference stations, rather than absolute values. To consider the reference stations in the linear system $\mathbf{f} = \mathbf{Hk}$, rows are appended to \mathbf{H} , having a value of 1 for a column indicating the reference station, and otherwise, 0. For \mathbf{f} , extended rows have a value of zero, representing zero site response at the reference stations. If there are more than one observation for a two-station-two-event pair, the average of all the right-hand side values from the observations is used as a \mathbf{f} value for the pair. The system then is inverted via the same method as in the $Lg Q$ inversion.

5. Results

5.1. RTSM Results

Figure 4 shows relative site responses at center frequencies of 0.75, 1, 2 and 2.75 Hz obtained using the RTSM. Since RTSM yields site response values relative to the reference stations, selecting an appropriate set of reference is critical. Gallegos et al. (2017) suggested that utilizing more than a single station as reference station is likely to ensure more reliable solution. We tested for the effect of the choice of reference stations, and found that only the level of amplitudes changed while the distribution of the site response appears to be robust regardless of the reference stations (Figure S7 in Supporting Information S1). In terms of the amplitude, it is recommended to select stations that are assumed to be free from both amplification and de-amplification, and general rock sites are often considered to satisfy the assumption. We chose two stations (CC03 and CC38) as the reference (Figure 7a), which are closest to the general rock site based on the site classification of National Earthquake Hazards Reduction Program (NEHRP; Table S3 in Supporting Information S1). Note that the terms “amplification” and “de-amplification” used for the rest of this paper are relative to the two reference stations, and might not always indicate amplification or de-amplification in absolute sense.

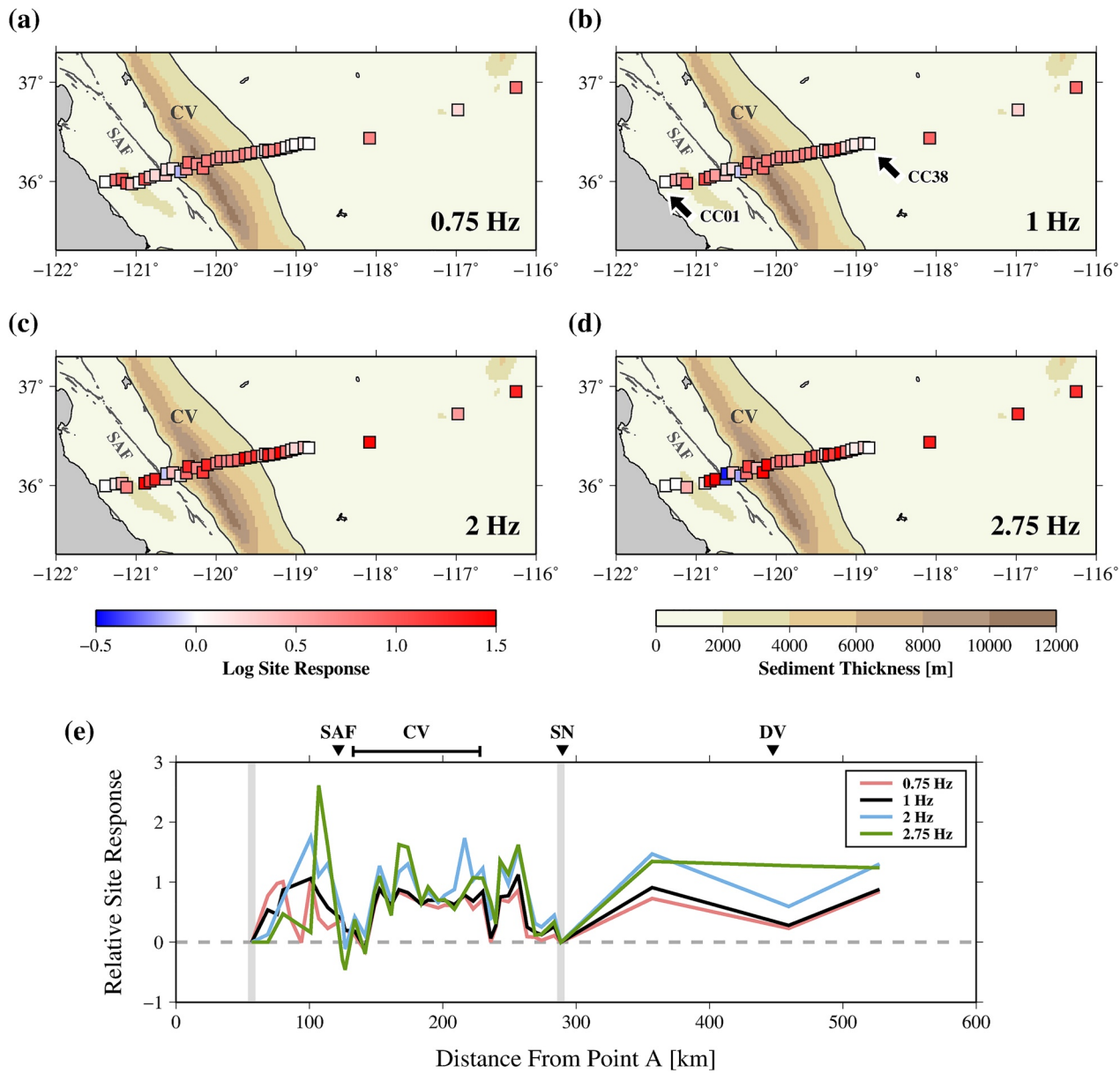


Figure 4. Relative site responses centering at (a) 0.75 Hz, (b) 1 Hz, (c) 2 Hz, and (d) 2.75 Hz, with the thickness of the sediments (Mooney & Kaban, 2010), and (e) comparison of relative site responses at each frequency. Contour lines indicate CV and gray lines in (a-d) represent SAF. CC03 and CC38 are used as reference stations, as indicated by the black arrows in (b) and gray vertical lines in (e). Most of the stations exhibit positive site responses, indicating the presence of soft surficial material at the region. Stronger amplification is observed at younger sedimentary region including the CV while weak to moderate de-amplification is observed at the east of the SAF. (SAF: San Andreas Fault, CV: Central Valley, SN: Starting point for the Sierra Nevada, DV: Death Valley).

At all frequencies, positive site response values (i.e., amplification) are obtained from most of the stations, reflecting pervasive sedimentary rocks present at the surface of the region. At 0.75 and 1 Hz, site responses show a similar pattern: strong positive site responses (~ 1.0) are observed in the regions filled with unconsolidated or loosely consolidated sedimentary deposits (e.g., CV), and weak negative values of about -0.1 (i.e., de-amplification) are obtained at the western edge of the basin (e.g., station CC15). At 2 and 2.75 Hz, both amplification and de-amplification become more striking compared to the lower frequencies. Stronger positive site responses (>1.5) are observed in sedimentary regions. At the westernmost part of the CV, weak (~ -0.1) and moderate (~ -0.5) negative site responses are obtained for 2 and 2.75 Hz, respectively. At all frequencies, weak positive values (<0.5) are observed at the eastern end of the CCSE array, where it begins to meet the mountain range (i.e.,

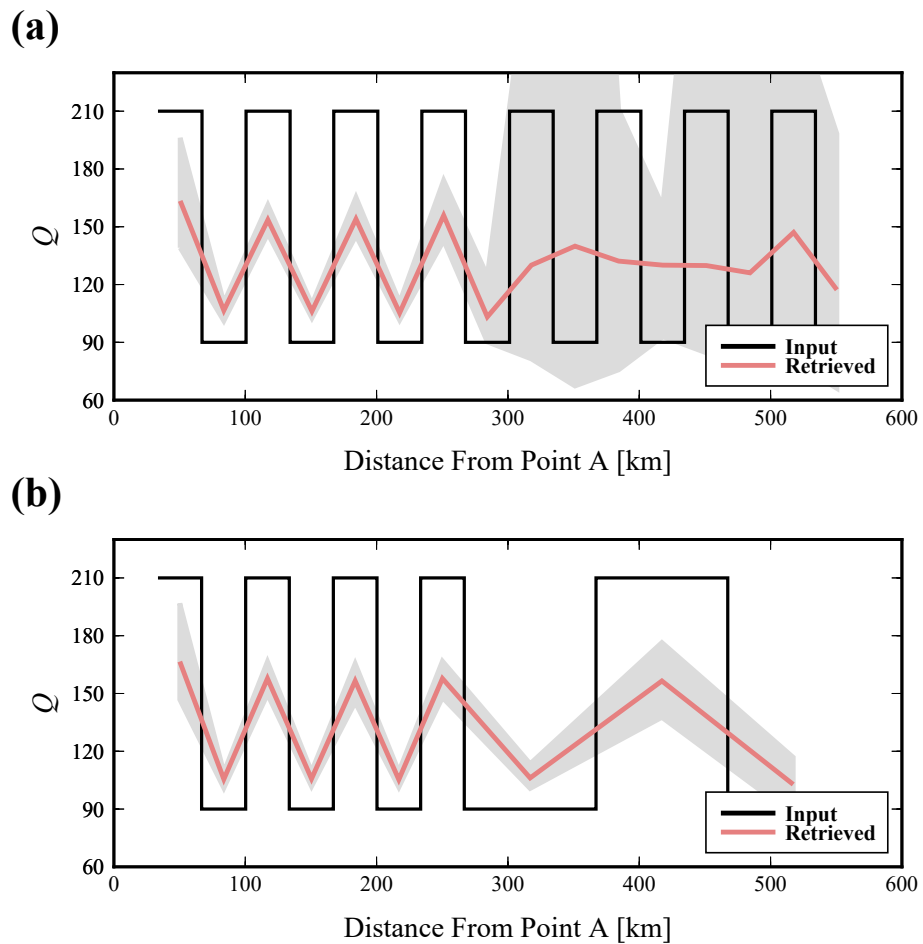


Figure 5. One-dimensional checker-board resolution test result with (a) a uniform grid size of 0.3° and (b) two different grid sizes of 0.3° and 0.9° . Black line signifies input Q structure with 40% perturbation and pink line indicates the average of the retrieved pattern. Gray shade represents the extent of fluctuation after 100 times of repeated test. Note that both mean Q values (pink lines) and the level of fluctuation (gray shades) are greatly improved when adopting the two different grid sizes considering the station density.

Sierra Nevada). We do not observe any relationship to the topography from the result, unlike the central-eastern US where strong coherence between the two is observed (Yassminh et al., 2019).

To ensure the reliability of the result, we checked how many rays hit at each station (Figure S8 in Supporting Information S1) and estimated uncertainty range of site response values after 500 time of bootstrapping (Figure S9 in Supporting Information S1). The uncertainties are generally low enough to support the robustness of the estimates. Ray hits are lower at the western (<100 km) and eastern (>450 km) edges of the profile, being as low as ~ 50 at lower frequencies and as ~ 25 at higher frequencies. A larger amount of rays ($>1,000$ at lower frequencies and ~ 500 at higher frequencies) traverses the stations between 100 and 450 km. Although the ray hit counts are low at <100 km, the ray coverage is still sufficient enough to attain stable inversion results. The incorporation of events at north and south directions ensured sufficient ray hit, even for the westernmost stations.

5.2. One-Dimensional Checker-Board Resolution Test Result

We assessed the resolution of the inversion result by the one-dimensional (1-D) checker-board test. For the test, we used an initial Q model centering at 150 with alternating $\pm 40\%$ perturbations for each cell (Figure 5). Based on the model, synthetic interstation Q data are generated with $\pm 10\%$ random noise, using the TSM. Since the TSM is sensitive to the input data, the random noise results in a slight fluctuation when retrieving the input perturbation. To compensate for the fluctuation, we repeated the test for 100 times and took an average.

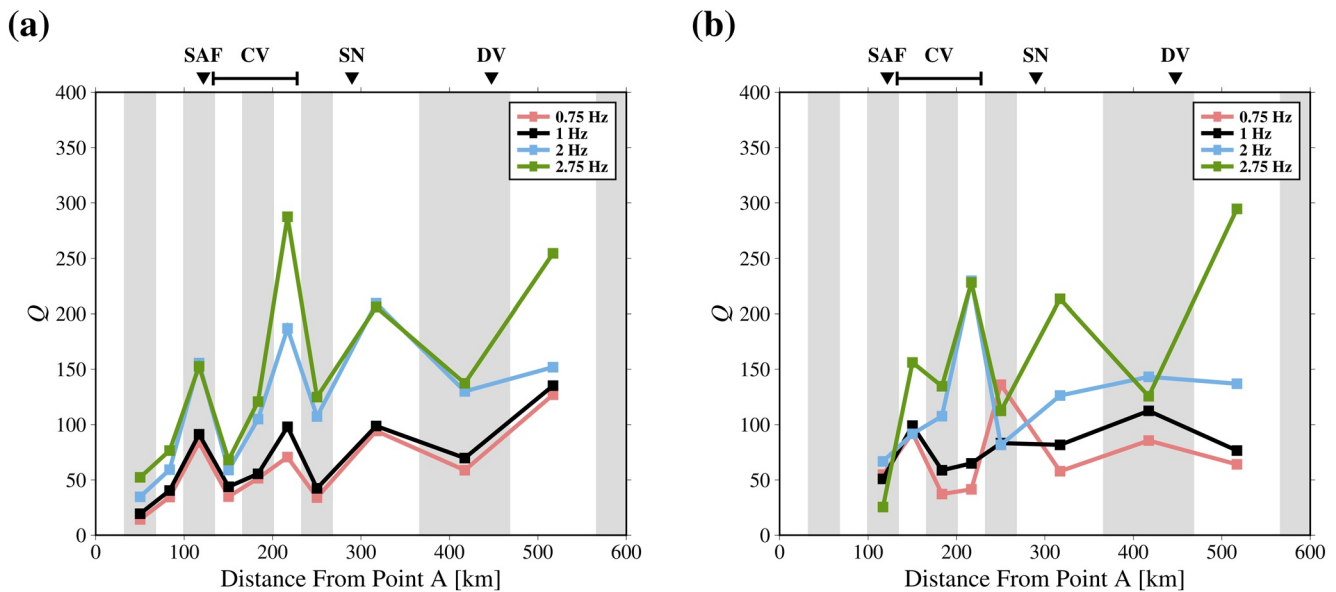


Figure 6. Lateral variation of $Lg Q$ along the A–A' profile based on (a) conventional two-station method (TSM) and (b) site-response-corrected TSM. Background gray and white colors denote the inversion grids. Note for the considerable change in the peak location after the correction. Black inverted triangles and a bar on top of each panel indicate locations of major geological features with their abbreviations (SAF: San Andreas Fault, CV: Central Valley, SN: Starting point for the Sierra Nevada, DV: Death Valley).

We observed that using a uniform cell size in the inversion results in a poor resolution for the regions farther than 250 km, the easternmost point of the CCSE array (Figure 5a). Not only the average of retrieved Q structures highly deviates from the input but also the level of fluctuation becomes severe. Based on its spatial correlation, we attribute this loss of resolution to a discrepancy in the station density: the average interstation distance within the CCSE array is ~ 6.5 km whereas it is ~ 23.7 km outside the array. Thus, we used a cell size of 0.3° for the first 250 km region covered by the CCSE array and a larger cell size of 0.9° for the farther region covered by the CI and SN stations. Adopting the different cell sizes considering the station density enhanced resolution for both regions (Figure 5b).

5.3. TSM Results

Figure 6a shows lateral variation of $Lg Q$ along the profile (A–A') using the conventional TSM. The inversion results are obtained after 31–44 iterations, with variance reductions ranging from 65.24% to 79.81% (Table 1). $Lg Q$ estimates tend to increase as the frequency increases: average Q value increases from 60.31 at 0.75 Hz to 147.97 at 2.75 Hz. The distribution of the $Lg Q$ exhibits similar pattern at all frequencies, with about three high- Q peaks along the profile at ~ 117 km, 217 km and 317 km from the point A. Also, Q values overall increase gently from the coast to the inland. For convenience, we shall use the term “uncorrected” for the rest of the paper to refer to the result obtained by the conventional TSM.

We then corrected the Q estimates for the site response term, using our estimates (Figure 6b). Compared to the uncorrected result, the number of iterations slightly decreased to 15–25 with increased variance reductions from 74.08% to 78.79% (Table 1), while the average Q value slightly increased at all frequencies. General trend of $Lg Q$ changed after the correction, which was more striking at lower frequencies (0.75 and 1 Hz) than the higher frequencies (2 and 2.75 Hz). Similar to the uncorrected result, the $Lg Q$ values increase as the center frequency increases and also show the increasing trend from west to east. Notable difference to the uncorrected result is the inconsistency of peak locations at the four frequencies. Peak location is similar for the lower frequencies (0.75 and 1 Hz), being at ~ 150 , 250 and 417 km east from the point A, while peaks lie at ~ 217 and 317 km from the point at 2.75 Hz. An intermediate behavior is obtained at 2 Hz: a peak at ~ 217 km follows the pattern at 2.75 Hz, while a gentle increase after ~ 250 km from the point A follows neither the lower nor the higher frequencies.

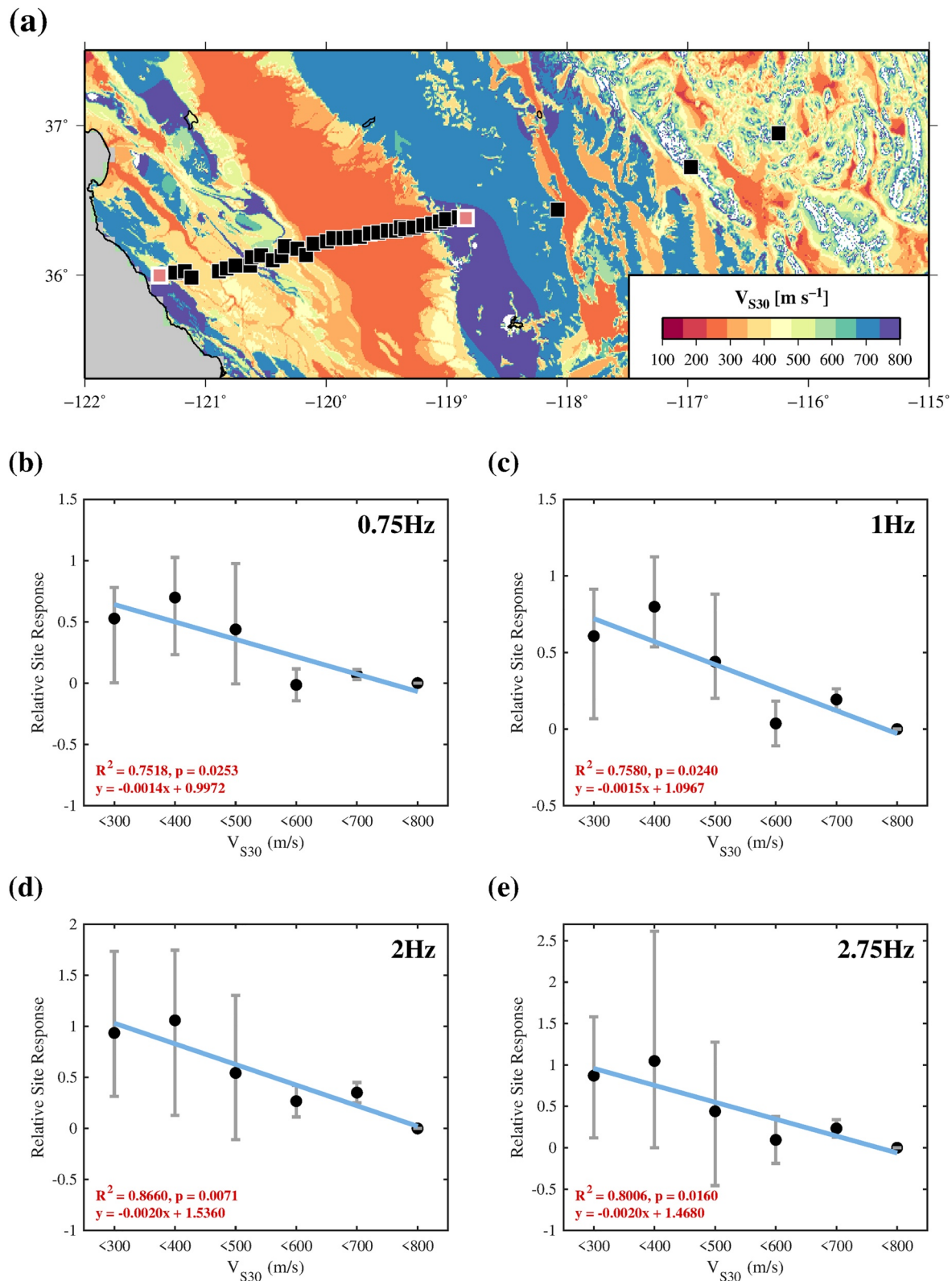


Figure 7. Relative site response and its correlation to the V_{S30} structure. (a) A map view of V_{S30} distribution in the study area (Heath et al., 2020). Black squares represent the stations used in this study, and the pink squares indicate the reference stations (i.e., CC03 and CC38). (b–e) Correlation between the site response and interval-averaged V_{S30} structure. Gray bar indicates the range of true values in the interval. Square of the correlation coefficients (R^2), p -values and the relation are provided at the left bottom corner of each panel.

Table 1

Summary of the TSM Result, Before and After the Correction

	Before correction			After correction		
	VR (%)	# It. (times)	Mean Q	VR (%)	# It. (times)	Mean Q
0.75 Hz	79.81	44	60.31	78.79	20	71.16
1 Hz	79.46	34	69.41	78.16	15	78.34
2 Hz	72.98	31	119.83	74.08	25	122.90
2.75 Hz	65.24	32	147.97	74.37	25	161.27

Note. Variance reduction (VR), the number of iteration to the solution (# It.) and the mean Q value at each frequency are presented.

We performed bootstrap sampling 500 times for the uncertainty range of the site-response-corrected $Lg Q$ estimates (Figure 8). The level of uncertainty tends to be elevated at higher frequencies. Considering that the Q values are larger at higher frequencies, the larger uncertainty at these frequencies can be associated with the magnitude of Q . Xie et al. (2004) reported similar observation and suggested that both larger interstation Q value and larger Q_m value may contribute to large uncertainty for Q at high frequency due to the way they are measured. Regardless of the level of uncertainty observed, the lateral pattern of $Lg Q$ variation along the profile is undisturbed by the selection of samples, which indicates the robustness of the pattern.

6. Discussion

6.1. Relative Site Response Along the CCSE Array

Two notable features from the result are the strong amplification in the sedimentary regions and the moderate de-amplification at the western edge of the basin, near the SAF. Regarding the amplification near the sedimentary basin, we found that a linear relationship between the level of amplification and the thickness of sediments is very weak. Rather, surface lithology and their degree of consolidation (<https://maps.conserv.ca.gov/cgs/gmc/App/>) seem to play more significant role in determining the level of amplification. Most of the stations that show strong amplification lie upon the Pleistocene-Holocene sedimentary rocks which are unconsolidated or semi-consolidated. In contrast, weak amplification is observed at either well-consolidated sedimentary regions or the regions with older lithology, mostly being Mesozoic. The other notable feature, which is the de-amplification at the western edge of the basin, might also be linked to the old and solid lithology distributed near the fault zone. Mesozoic Franciscan complex and well-consolidated sedimentary rocks are present east to the SAF, where negative site responses are obtained. The Franciscan complex is considered to be responsible for the low amplification found at north-eastern SAF by Phillips and Aki (1986), who estimated site effects in central California using coda waves. Based on their spatial correlation, we also attribute the site de-amplification at the edge of the basin to the metamorphosed or well-consolidated sedimentary rocks at the surface. The strong relation between site responses and the surface lithology (Borcherdt, 1970; Gallegos et al., 2017; Phillips & Aki, 1986; Rogers et al., 1979; Su et al., 1992) or the age of a rock (Su et al., 1992) has been reported by previous studies. Particularly for the western US, Gallegos et al. (2017) suggested that the influence of shallow geology might outstrip other aspects, such as radiation pattern or three-dimensional structure. Our observation strengthens previous reports and further emphasizes the significance of the consolidation status in massive sedimentary regions like the CV.

To understand the relationship between the site response and surface geology in a quantitative basis, we compared our result to the shear-wave velocity in the upper 30 m depth (i.e., V_{S30} ; Figure 7a; Heath et al., 2020). For the simplicity in comparison, we grouped the shear-wave velocity into an interval of 100 ms^{-1} , and used an average of the site response estimates within the interval. A strong negative correlation with the V_{S30} distribution is observed at all frequencies (Figure 7b), with high R^2 values (>0.7) and low p -values (<0.05). The relation can also be found in central-eastern US. Yassminh et al. (2019) observed a strong negative correlation between the two, reporting significant R^2 values of 0.56085 at 1 Hz and even larger (>0.87) at 2, 3 and 4 Hz. The result supports the reliability of our estimates, and highlights the close linkage between the site responses and surficial geology throughout the US.

We note that a larger variance in site response estimates is observed at slower V_{S30} , particularly at 2.75 Hz (Figure 7e). The large range of site response at slower V_{S30} regions might be attributed for (a) larger number of points (~ 16 points at $V_{S30} < 300$, ~ 10 points at $V_{S30} < 400$) compared to faster V_{S30} regions (~ 2 points), (b) lower sensitivity in V_{S30} data to the small-scale features due to the lack of measurement and associated interpolation while modeling V_{S30} , or (c) less accuracy in site response measurement at higher frequency, near 100 km.

Apart from the surficial effects, topography of a region (i.e., mountain ranges) can be closely linked with the site responses. Gallegos et al. (2017) reported negative site responses at Sierra Nevada mountain, being more prominent at 0.5 Hz than in higher frequencies, and Yassminh et al. (2019) observed a crucial influence of topography in determining the site responses in central-eastern US. However, we do not observe de-amplification at mountain

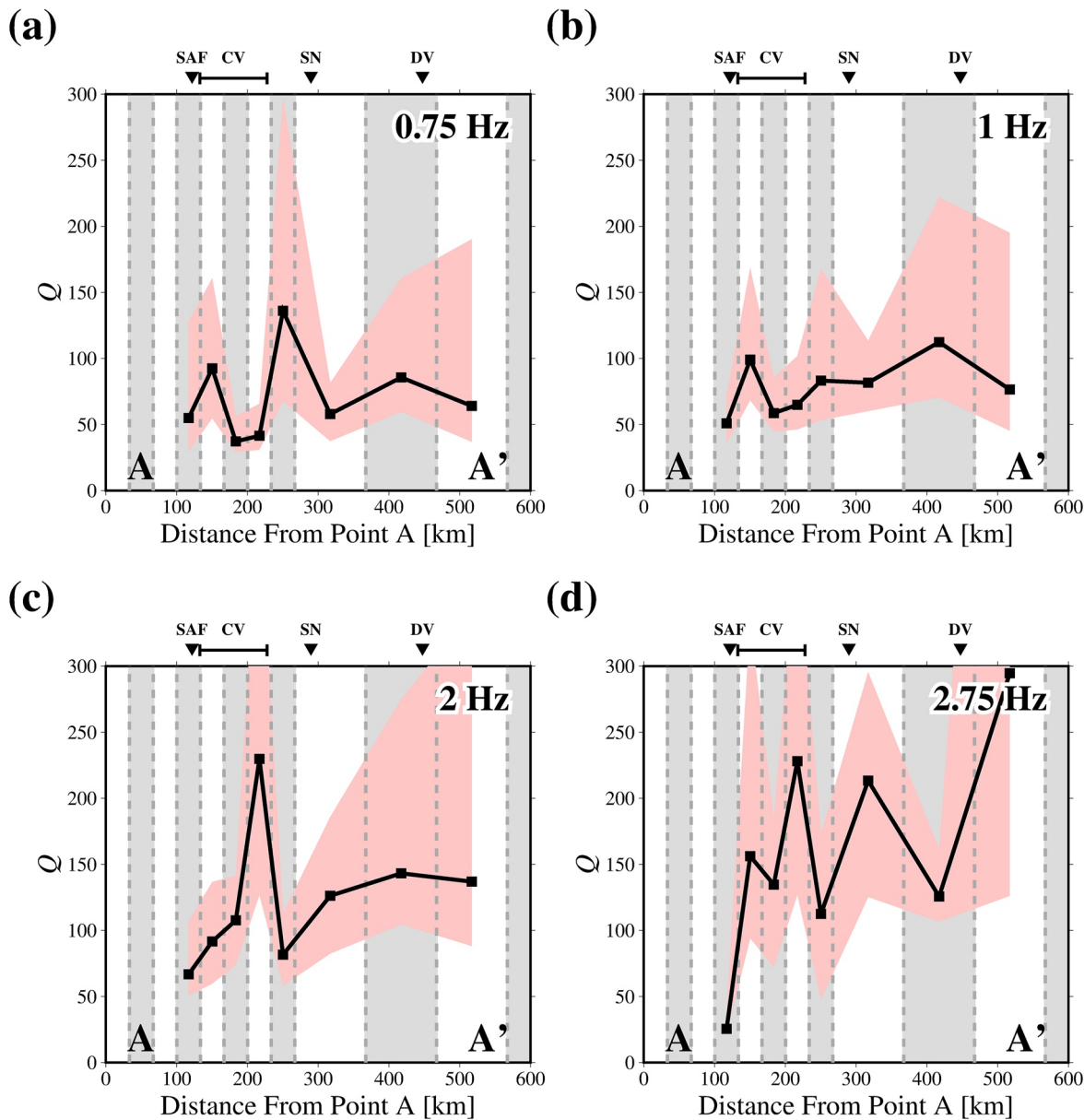


Figure 8. Spatial variation of the site-response corrected $Lg\ Q$ values, centering at (a) 0.75 Hz, (b) 1 Hz, (c) 2 Hz, and (d) 2.75 Hz. Pink shades indicate uncertainty ranges obtained after 500 times of bootstrapping. Background gray and white colors represent the location and width of the inversion grid. Black inverted triangles and a bar on top of each panel indicate locations of major geological features with their abbreviations (SAF: San Andreas Fault, CV: Central Valley, SN: Starting point for the Sierra Nevada, DV: Death Valley).

ranges or a clear relation to the topography. This might be attributed to the low station coverage at the easternmost part of the profile, where topography changes abruptly starting from the mountain range. Due to the lack of coverage, sensitivity to the topographic slope might not be imaged as sharply, or a narrow feature such as locally deposited sediments might block the general tendency of negative site response. On the other hand, topography might not be a more significant factor in controlling the site response in central California than the shallow geology. In order to clarify the effect of the mountain range, further investigation with a denser array data is necessary.

6.2. Comparison With Previous Studies

Our 1-D $Lg\ Q$ structure based on the site-response-corrected TSM, centered at 0.75, 1, 2, and 2.75 Hz (Figure 8), exhibits a clear frequency dependence of $Lg\ Q$, having lower average Q value of ~71 at 0.75 Hz and higher value

Table 2

Frequency Dependence of the Site-Response-Corrected $Lg Q$ Model. 95% Confidence Intervals for Each Average Q Value Are Indicated Inside the Parenthesis

	Average Q (95% confidence interval)
0.75 Hz	71.16 (± 29.08)
1 Hz	78.34 (± 18.34)
2 Hz	122.90 (± 45.45)
2.75 Hz	161.27 (± 73.86)

of ~ 161 at 2.75 Hz (Tables 1 and 2). At each frequency, Q values gradually become larger as moving toward inland. This increment might reflect the change in the stiffness of the rocks, from the soft marine accretionary wedges (Blake et al., 1988) to the hard granitic intrusions (Godfrey & Klemperer, 1998). We observe locally high Q values near the CV, and no clear peak near the Sierra Nevada, except for the high- Q peak observed at the highest frequency.

Previous $Lg Q$ studies coherently reported larger $Lg Q_0$ values (> 500) in tectonically stable central-eastern US and smaller values (80–350) in tectonically active western US, particularly being lowest near the Pacific coast. Our site-response-corrected TSM result at 1 Hz also gradually increases toward east, implying more stable condition in the central US. We obtained $Lg Q_0$

values ranging 50–100, obviously lower compared to the central-eastern US and even being the smallest among the estimates in western US. Considering the westernmost position of the profile used in this study and the decreasing trend of $Lg Q$ in the US from east to west, the lowest Q estimates seem to agree well with previous investigations. Such low value might reflect the existence of massive unconsolidated sedimentary deposits and presence of fluids in the upper crust that has been formed through past crustal and mantle heating (Baqer & Mitchell, 1998).

We obtained the frequency dependence of the $Lg Q$ values by best-fitting the mean Q values at each frequency (Table 2) in the Q - f domain (Figure S10 in Supporting Information S1), and its power-law frequency dependence is described as $Q(f) = (81 \pm 8)f^{(0.62 \pm 0.11)}$. In California, $Lg Q$ as a function of frequency has also been investigated by various researchers. Benz et al. (1997) inverted the Lg wave amplitude into source term, site term and Q term for every octave from 0.5 to 7.0 Hz. They obtained $Q(f) = (187 \pm 7)f^{(0.55 \pm 0.03)}$ between 1.0 and 7.0 Hz in southern-central California, and $Q(f) = (235 \pm 11)f^{(0.56 \pm 0.04)}$ between 1.0 and 5.0 Hz in Basin and Range Province. Similarly, Erickson et al. (2004) determined the Lg wave attenuation for the continental US centering at 0.75, 1, 3, 6 and 12 Hz. They inverted the Lg wave amplitude through singular value decomposition, and yielded frequency dependent $Lg Q$ of $Q(f) = (105 \pm 26)f^{(0.67 \pm 0.16)}$ for northern California and $Q(f) = (152 \pm 37)f^{(0.72 \pm 0.16)}$ for southern California. Gallegos et al. (2017) estimated the frequency dependence as $Q(f) = 97f^{0.25}$ and $Q(f) = 99f^{0.44}$ for southern and northern California, respectively. Again, we find our $Lg Q_0$ value of 81 falls within the lowermost range of the previous estimates. The η value of 0.62 shows a good agreement with the previously reports in California (0.25–0.72), while is notably higher than the measurements for central-northern US (0.344–0.36; Erickson et al., 2004), or northeastern US (0.22; Benz et al., 1997). High η value seems to highlight the strong tectonic activity of the region.

6.3. Effect of the Site Response Correction on $Lg Q$

$Lg Q$ values are often correlated with several crustal characteristics such as thick sediments (e.g., Gallegos et al., 2014; Mitchell & Hwang, 1987; Ranasinghe et al., 2015; Wei et al., 2017; Zhao & Mousavi, 2018), thermal conditions (e.g., Frankel, 1991), shear-wave velocity (e.g., Gallegos et al., 2017; Zhao & Mousavi, 2018), crustal thickness (e.g., Zhao et al., 2010; Zhao, Xie, He, et al., 2013) or partial melting in the crust (e.g., Xie et al., 2004). Here, we focus on the relationship with the sediments, shear-wave velocity structure and Moho temperature, which are most frequently linked with the attenuation structure in western US (Gallegos et al., 2017; Phillips & Stead, 2008).

First, we focused on the discrepancy between the uncorrected and corrected results (Figure 6). One of the interesting aspects from the corrected result is the inconsistency in the peak locations at each frequency. We suspect that the site-response-correction might sharpen the sensitivity of the measurement so that each frequency could highlight distinct part of the crust, which results in unique patterns for each frequency. This idea can be supported by an observation: a reversal of $Lg Q$ value near the CV. Between 130–200 km east from the point A, locally high Q value of ~ 100 is obtained after the correction in contrast to the locally low Q value of ~ 50 before the correction. In previous sections, we observed that site response is closely related to surficial properties, particularly with sediments. Thick layer of sediments at the surface is one of the major contributors to the low $Lg Q$ value (Hong, 2010; Mitchell & Hwang, 1987; Wei et al., 2017; Zhao & Mousavi, 2018; Zhao et al., 2010). The rise of $Lg Q$ value at CV after the correction can be considered as a loss of low- Q contributor due to the correction.

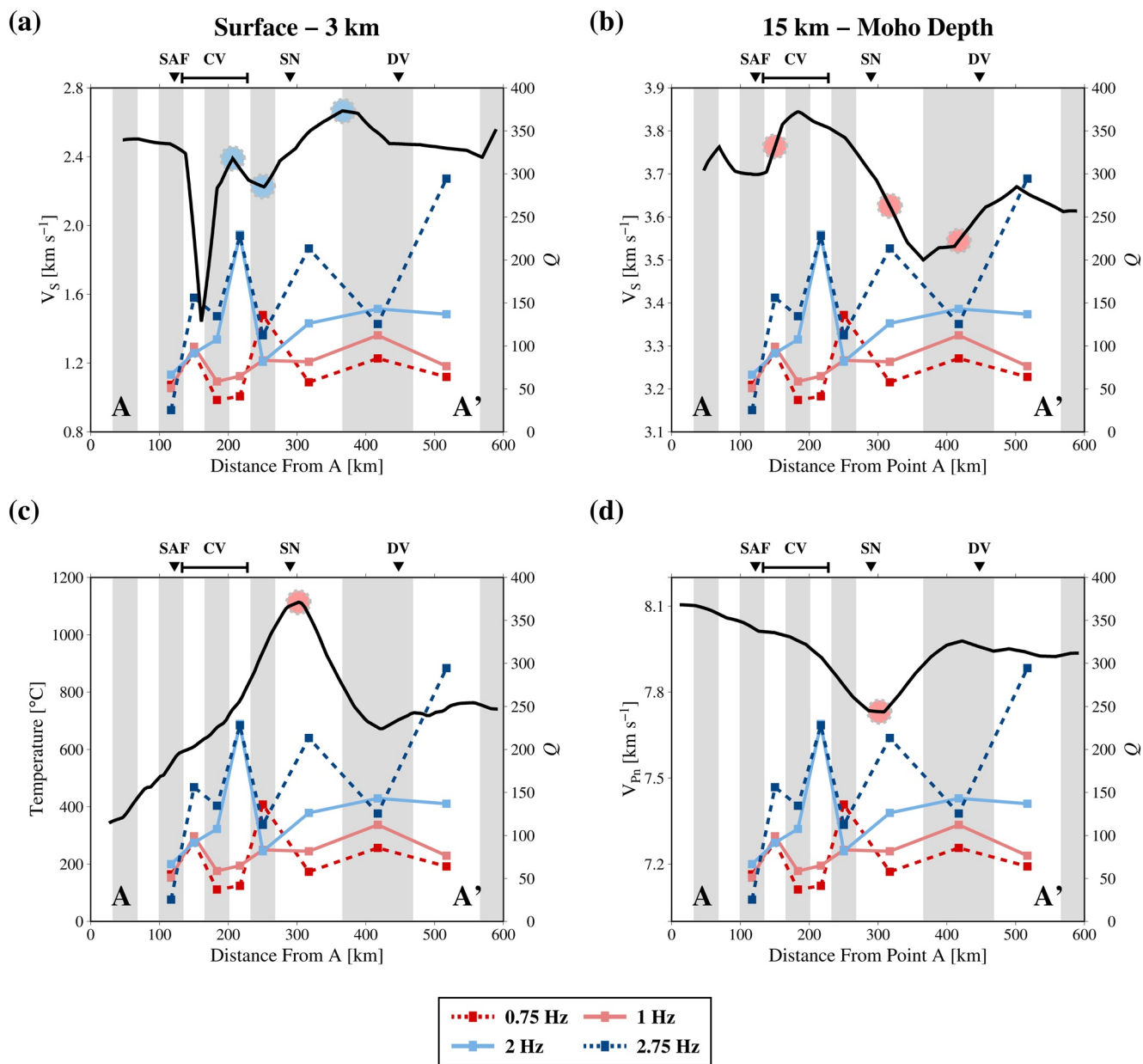


Figure 9. Geologic and geophysical properties along the A–A' profile and their comparison to the Lg Q variation. (a) Shallow and (b) deep shear-wave velocity variation (Shen et al., 2013), (c) Moho temperature (Schutt et al., 2018) and (d) Pn velocity structure (Buehler & Shearer, 2017) along the profile. Red circles denote the features related to the lower frequency results (0.75 and 1 Hz) while the blue circles indicate the relation to the higher frequency results (2 and 2.75 Hz). Black inverted triangles and a bar on top of each panel indicate locations of major geological features with their abbreviations (SAF: San Andreas Fault, CV: Central Valley, SN: Starting point for the Sierra Nevada, DV: Death Valley).

Considering the close linkage between the site responses and surface properties, the sediments at the surface are likely to be the contributor. Thus, we suggest that the correction of site term might minimize the effect of the massive sediments at the surface and reveal a deeper structure beneath the basin. In other words, the site-response-correction might introduce a possibility to image more diverse depth ranges of the Lg wave attenuation structure, particularly in combination with the use of various frequencies. We note that the reversal of Q values near CV is more striking at lower frequencies (0.75 and 1 Hz), indicating that the effect of the correction is less critical at higher frequencies.

To better understand the depth resolution introduced by the correction, we compared our site-response-corrected Lg Q result with the shear-wave velocity (V_s) structure (Figures 9a and 9b). In central California, a strong contrast

in shallow and deep shear-wave velocity has been reported by several previous studies (Jiang et al., 2018; Shen et al., 2013), particularly beneath the central CV: V_s being $\sim 1.4 \text{ km s}^{-1}$ near the surface, while $\sim 3.9 \text{ km s}^{-1}$ near the Moho (Shen et al., 2013). The extremely low shear-wave velocity near the surface of the valley can be mainly attributed to the thick sediments, most of which are not fully consolidated. The origin of the imaged high velocity structure beneath the CV is still under debate: it is interpreted either as a remnant of an underthrust oceanic lithosphere (Wang et al., 2013) or as a relic of an ancient craton (Shen et al., 2013) whereas Godfrey and Klemperer (1998) and Fliedner et al. (2000) considered it as an extension of the great valley ophiolite. Moreover, based on their spatial correlation, we also note for the possible connection between the high- V_s structure at the lower crust and the Isabella anomaly, as suggested by Jiang et al. (2018). It is well known that a region of low shear-wave velocity tends to exhibit a low $Lg Q$ value, and vice versa (Gallegos et al., 2017; Zhao & Mousavi, 2018). Considering the striking contrast, we isolated the V_s structure provided by Shen et al. (2013) into the shallower (upper 3 km) part and the deeper (15 km to a depth of Moho) part (Figures 9a and 9b). We observed that the pattern at lower frequencies (0.75 and 1 Hz) seem to resemble some notable changes in the deep V_s structure (red circles Figure 9) while the shallower V_s structure seems to be imaged by higher frequencies (blue circles in Figure 9).

Relations to the Moho temperature (Figure 9c; Schutt et al., 2018) and Pn velocity structure (Figure 9d; Buehler & Shearer, 2017) also support the depth sensitivity by frequency. Along the A–A' profile, Moho temperature gradually increases from the coast to a distance of ~ 300 km and then gently decreases as moving further inland. The Pn velocity structure shows a reversed relationship to the Moho temperature variation as it mostly travels along the crust-mantle boundary, being affected by the properties of the Moho (Schutt et al., 2018). An inversely proportional relationship between the temperature and the $Lg Q$ values is generally expected considering the strong attenuation of the Lg wave caused by the high temperature (Frankel, 1991; Wei et al., 2017). At 0.75 Hz, a distinct low- Q peak is imaged at the point of the maximum Moho temperature and minimum Pn velocity, while the peak is still observable at 1 Hz but not as much striking as at 0.75 Hz (red circles in Figure 9). Contrastingly, the effect of Moho temperature seems to be insignificant at higher frequencies, with no clear peak at 2 Hz or even with a high- Q peak at 2.75 Hz. The result strengthens the possible linkage between the deeper structure and the lower frequency.

From the comparison to the regional geology, we find that the site-response-correction is indeed effective for removing the surficial properties, leading to a consistent relationship of deeper geologic features to the $Lg Q$ estimates at lower frequency, and vice versa. Although $Lg Q$ is often understood as the crustal averaged property (Xie et al., 2004), efforts to image diverse depth range of the crust using Lg waves of different frequencies has been made (e.g., Wei et al., 2017). Our result supports the idea that the Lg wave attenuation might have a depth sensitivity, and suggests that it can be reinforced through the site-response-correction by removing the surficial properties. Recalling the relation with the shear-wave velocity structure, lower frequencies (0.75 and 1 Hz) seem to be strongly affected by the lower crust, particularly lower than ~ 15 km. Among the two, 0.75 Hz seems to image even deeper structure, close to the Moho depth, considering the comparison with Moho temperature. Higher frequencies (2 and 2.75 Hz) seem to have the potential to image shallower part of the crust, possibly less than ~ 3 km depth. The intimate relation between the $Lg Q$ variation at higher frequencies and the shallow shear-wave velocity structure supports the idea. The sensitivity to the shallower structures at these frequency ranges is also reflected by the insignificant changes in the $Lg Q$ structure before and after the correction. Since the result from 2 Hz exhibits intermediate behavior between 1 and 2.75 Hz result, we speculate that the center frequency of 2 Hz might be sensitive to upper-to-middle crust. This result raises the possibility of more sophisticated surveys on crustal characteristics using the Lg wave, highlighting the necessity of quantification on the detailed depth resolution of $Lg Q$ in the near future, possibly through a synthetic full-waveform inversion.

7. Conclusions

We estimated lateral variation of the $Lg Q$ along a great circle profile along the CCSE array, crossing SAF and CV, at four center frequencies (0.75, 1, 2 and 2.75 Hz) and also obtained relative site responses at each station. The relative site responses were dominantly positive, reflecting the widespread sedimentary rocks along the profile. The relative site responses exhibit a higher association to the age or consolidation status of the surface lithology, rather than the thickness of sediments. Furthermore, the site responses are strongly correlated to the V_{S30} , supporting the intimate connection between the site terms and the surface geology.

We modified conventional TSM by correcting for the site response term with our estimates, and compared the result with conventional TSM. Regardless of the correction, $Lg Q$ values increased from the western coast to the inland, reflecting the change in regional lithology from soft sediments to hard igneous rocks. However, peak locations from the $Lg Q$ profile shifted after the site-response-correction, and the change was more prominent at lower frequencies (0.75 and 1 Hz) than at higher frequencies (2 and 2.75 Hz). The site-response corrected $Lg Q$ values tend to increase as the center frequency increases, following a power-law frequency dependence of $Q(f) = (81 \pm 8)f^{(0.62 \pm 0.11)}$. The estimate falls in a lowest range of the previously reported values, reflecting the high tectonic activity and the presence of fluids in the region. Locally high Q values are obtained near the CV, particularly at lower frequencies (0.75 and 1 Hz), rather than the expected low Q values. Shear-wave velocity values at deeper and shallower depths seem to be correlated with the $Lg Q$ structures at lower and higher frequencies, respectively, while the Moho temperature is inversely coherent only to the lower frequency results. Our results suggest that the correction effectively minimizes the strong surficial influences and helps imaging deeper structures (~15 km to the Moho depth).

Data Availability Statement

Seismic data used in this study are obtained from IRIS Data Management Center, including the CCSE array (<https://doi.org/10.7909/C3B56GVW>), CI network (<https://doi.org/10.7914/SN/CI>) and SN network (<https://doi.org/10.7914/SN/SN>) data. Geologic map is downloaded from the U.S. Geological Survey (USGS) website available at <https://mrdata.usgs.gov/geology/state/> (last accessed February 2020). The Pn velocity and the Moho depth data are obtained from the IRIS Earth Model Collaboration website at <http://ds.iris.edu/ds/products/emc-earthmodels/> (last accessed September 2020). The V_{S30} data is available at USGS Earthquake Hazards Program (<https://earthquake.usgs.gov/data/vs30/>; last accessed April 2021), and the V_s model is downloaded from the author's webpage at <http://ciei.colorado.edu/Models/> (last accessed February 2020). All figures in this article are generated using the GMT (<https://www.generic-mapping-tools.org/>) and MATLAB.

Acknowledgments

J. Yun and Y. Kim acknowledge the National Research Foundation of Korea (NRF) grant funded by the Korea government (MSIT; No. NRF-2019R1G1A1094833), and the funding from Development of unified 3-D seismic velocity model program (KMI2019-00110) through Korea Meteorological Administration. Finally, the authors thank Editor Maureen Long, Dr. Nishath Rajiv Ranasinghe, and an anonymous reviewer for comments which greatly improved this paper.

References

- Bao, X., Sandvol, E., Ni, J., Hearn, T., Chen, Y. J., & Shen, Y. (2011). High resolution regional seismic attenuation tomography in eastern Tibetan Plateau and adjacent regions. *Geophysical Research Letters*, 38, L16304. <https://doi.org/10.1029/2011gl048012>
- Baer, S., & Mitchell, B. J. (1998). Regional variation of Lg coda Q in the continental United States and its relation to crustal structure and evolution. In *Q of the Earth: Global, regional, and laboratory studies* (pp. 613–638). Birkhäuser. https://doi.org/10.1007/978-3-0348-8711-3_17
- Becken, M., Ritter, O., Park, S. K., Bedrosian, P. A., Weckmann, U., & Weber, M. (2008). A deep crustal fluid channel into the San Andreas Fault system near Parkfield, California. *Geophysical Journal International*, 173, 718–732. <https://doi.org/10.1111/j.1365-246x.2008.03754.x>
- Bennington, N., Thurber, C., & Roecker, S. (2008). Three-dimensional seismic attenuation structure around the SAFOD site, Parkfield, California. *Bulletin of the Seismological Society of America*, 98(6), 2934–2947. <https://doi.org/10.1785/0120080175>
- Benz, H. M., Frankel, A., & Boore, D. M. (1997). Regional Lg attenuation for the continental United States. *Bulletin of the Seismological Society of America*, 87, 606–619. <https://doi.org/10.1785/bssa0870030606>
- Blake, M. C., Jr, Jayko, A. S., McLaughlin, R. J., & Underwood, M. B. (1988). Metamorphic and tectonic evolution of the Franciscan Complex, northern California. In W. G. Ernst (Ed.), *Metamorphism and crustal evolution of the Western United States* (pp. 1035–1060). Prentice-Hall
- Blandford, R. R. (1981). Seismic discrimination problems at regional distances. In *Identification of seismic sources—Earthquake or underground explosion* (pp. 695–740). Springer. https://doi.org/10.1007/978-94-009-8531-5_38
- Borchert, R. D. (1970). Effects of local geology on ground motion near San Francisco Bay. *Bulletin of the Seismological Society of America*, 60, 29–61
- Bouchon, M. (1982). The complete synthesis of seismic crustal phases at regional distances. *Journal of Geophysical Research: Solid Earth*, 87, 1735–1741. <https://doi.org/10.1029/jb087ib03p01735>
- Boyd, O. S., Jones, C. H., & Sheehan, A. F. (2004). Foundering lithosphere imaged beneath the southern Sierra Nevada, California, USA. *Science*, 305, 660–662. <https://doi.org/10.1126/science.1099181>
- Buehler, J. S., & Shearer, P. M. (2017). Uppermost mantle seismic velocity structure beneath USArray. *Journal of Geophysical Research: Solid Earth*, 122, 436–448. <https://doi.org/10.1002/2016jb013265>
- Chun, K. Y., West, G. F., Kokoski, R. J., & Samson, C. (1987). A novel technique for measuring Lg attenuation—Results from eastern Canada between 1 to 10 Hz. *Bulletin of the Seismological Society of America*, 77, 398–419. <https://doi.org/10.1785/bssa0770020398>
- Der, Z. A., Marshall, M. E., O'Donnell, A., & McElfresh, T. W. (1984). Spatial coherence structure and attenuation of the Lg phase, site effects, and the interpretation of the Lg coda. *Bulletin of the Seismological Society of America*, 74, 1125–1147.
- Dougherty, S. L., Jiang, C., Clayton, R. W., Schmandt, B., & Hansen, S. M. (2021). Seismic evidence for a fossil slab origin for the Isabella anomaly. *Geophysical Journal International*, 224, 1188–1196.
- Eberhart-Phillips, D. (2016). Northern California seismic attenuation: 3D QP and QS models. *Bulletin of the Seismological Society of America*, 106, 2558–2573.
- Eberhart-Phillips, D., & Michael, A. J. (1993). Three-dimensional velocity structure, seismicity, and fault structure in the Parkfield region, central California. *Journal of Geophysical Research*, 98, 15737–15758.
- Eberhart-Phillips, D., Thurber, C., & Fletcher, J. B. (2014). Imaging P and S attenuation in the Sacramento–San Joaquin delta region, northern California. *Bulletin of the Seismological Society of America*, 104, 2322–2336.

- Erickson, D., McNamara, D. E., & Benz, H. M. (2004). Frequency-dependent Lg Q within the continental United States. *Bulletin of the Seismological Society of America*, 94, 1630–1643. <https://doi.org/10.1785/012003218>
- Farrar, C. D., & Bertoldi, G. L. (1988). Region 4, Central Valley and Pacific coast ranges. In W. Back, J. S. Rosenshein, & P. R. Seaber (Eds.), *Hydrogeology: The geology of North America* (pp. 59–67). Geological Society of America
- Fliedner, M. M., Klemperer, S. L., & Christensen, N. I. (2000). Three-dimensional seismic model of the Sierra Nevada arc, California, and its implications for crustal and upper mantle composition. *Journal of Geophysical Research*, 105(B5), 10899–10921. <https://doi.org/10.1029/2000JB900029>
- Ford, S. R., Dreger, D. S., Mayeda, K., Walter, W. R., Malagnini, L., & Phillips, W. S. (2008). Regional attenuation in northern California: A comparison of five 1D Q methods. *Bulletin of the Seismological Society of America*, 98(4), 2033–2046. <https://doi.org/10.1785/0120070218>
- Frankel, A. (1991). Mechanisms of seismic attenuation in the crust: Scattering and anelasticity in New York State, South Africa, and southern California. *Journal of Geophysical Research*, 96, 6269–6289. <https://doi.org/10.1029/91jb00192>
- Gallegos, A., Ranasinghe, N., Ni, J., & Sandvol, E. (2014). Lg attenuation in the central and eastern United States as revealed by the EarthScope Transportable Array. *Earth and Planetary Science Letters*, 402, 187–196. <https://doi.org/10.1016/j.epsl.2014.01.049>
- Gallegos, A., Ranasinghe, N., Ni, J., & Sandvol, E. (2017). Lg attenuation, frequency dependence and relative site response of the western United States as revealed by the EarthScope Transportable Array. *Geophysical Journal International*, 209, 1955–1971. <https://doi.org/10.1093/gji/ggx145>
- Gavin, P. (2019). *The Levenberg-Marquardt algorithm for nonlinear least squares curve-fitting problems* (Vol. 10). Department of Civil and Environmental Engineering Duke University.
- Godfrey, N. J., Beaudoin, B. C., & Klemperer, S. L. (1997). Ophiolitic basement to the Great Valley forearc basin, California, from seismic and gravity data: Implications for crustal growth at the North American continental margin. *The Geological Society of America Bulletin*, 109, 1536–1562. [https://doi.org/10.1130/0016-7606\(1997\)109<1536:obttgv>2.3.co;2](https://doi.org/10.1130/0016-7606(1997)109<1536:obttgv>2.3.co;2)
- Godfrey, N. J., & Klemperer, S. L. (1998). Ophiolitic basement to a forearc basin and implications for continental growth: The Coast Range/Great Valley ophiolite, California. *Tectonics*, 17, 558–570. <https://doi.org/10.1029/98tc01536>
- Hasegawa, H. S. (1985). Attenuation of Lg waves in the Canadian shield. *Bulletin of the Seismological Society of America*, 75, 1569–1582.
- He, J., Sandvol, E., Wu, Q., Gao, M., Gallegos, A., Ulziibat, M., & Demberel, S. (2017). Attenuation of regional seismic phases (Lg and Sn) in Eastern Mongolia. *Geophysical Journal International*, 211, 979–989. <https://doi.org/10.1093/gji/ggx349>
- Heath, D. C., Wald, D. J., Worden, C. B., Thompson, E. M., & Smoczyk, G. M. (2020). A global hybrid V_{S30} map with a topographic slope-based default and regional map insets. *Earthquake Spectra*, 36, 1570–1584. <https://doi.org/10.1177/8755293020911137>
- Hong, T. K. (2010). Lg attenuation in a region with both continental and oceanic environments. *Bulletin of the Seismological Society of America*, 100, 851–858. <https://doi.org/10.1785/0120090057>
- Jennings, C. W., Strand, R. G., & Rogers, T. H. (1977). *Geologic map of California* (Vol. 1, p. 750). California Division of Mines and Geology, scale 1:750,000.
- Jiang, C., Schmandt, B., Hansen, S. M., Dougherty, S. L., Clayton, R. W., Farrell, J., & Lin, F. C. (2018). Rayleigh and S wave tomography constraints on subduction termination and lithospheric foundering in central California. *Earth and Planetary Science Letters*, 488, 14–26. <https://doi.org/10.1016/j.epsl.2018.02.009>
- Kennett, B. L. N. (1983). *Seismic wave propagation in stratified media*. Cambridge University Press.
- Kennett, B. L. N. (1986). Lg waves and structural boundaries. *Bulletin of the Seismological Society of America*, 76, 1133–1141.
- Knopoff, L., Schwab, F., & Kausel, E. (1973). Interpretation of Lg. *Geophysical Journal International*, 33, 389–404. <https://doi.org/10.1111/j.1365-246x.1973.tb02375.x>
- Levenberg, K. (1944). A method for the solution of certain non-linear problems in least squares. *Quarterly of Applied Mathematics*, 2, 164–168. <https://doi.org/10.1090/qam/1066>
- Marquardt, D. W. (1963). An algorithm for least-squares estimation of nonlinear parameters. *Journal of the Society for Industrial and Applied Mathematics*, 11, 431–441. <https://doi.org/10.1137/0111030>
- Mitchell, B. J. (1995). Anelastic structure and evolution of the continental crust and upper mantle from seismic surface wave attenuation. *Reviews of Geophysics*, 33, 441–462. <https://doi.org/10.1029/95rg02074>
- Mitchell, B. J., Cong, L., & Jemberie, A. L. (2015). Continent-wide maps of Lg coda Q for North America and their relationship to crustal structure and evolution. *Bulletin of the Seismological Society of America*, 105, 409–419. <https://doi.org/10.1785/0120130235>
- Mitchell, B. J., & Hwang, H. J. (1987). Effect of low Q sediments and crustal Q on Lg attenuation in the United States. *Bulletin of the Seismological Society of America*, 77, 1197–1210. <https://doi.org/10.1785/bssa0770041197>
- Mitchell, B. J., Pan, Y., Xie, J., & Cong, L. (1997). Lg coda Q variation across Eurasia and its relation to crustal evolution. *Journal of Geophysical Research: Solid Earth*, 102, 22767–22779. <https://doi.org/10.1029/97jb01894>
- Mooney, W. D., & Kaban, M. K. (2010). The North American upper mantle: Density, composition, and evolution. *Journal of Geophysical Research: Solid Earth*, 115. <https://doi.org/10.1029/2010jb000866>
- Noriega, R., Ugalde, A., Villaseñor, A., & Jurado, M. J. (2015). Spatial variation of Lg-wave attenuation in the Iberian Peninsula. *Bulletin of the Seismological Society of America*, 105, 420–430. <https://doi.org/10.1785/0120140045>
- Nuttli, O. W. (1973). The Mississippi Valley earthquakes of 1811 and 1812: Intensities, ground motion and magnitudes. *Bulletin of the Seismological Society of America*, 63, 227–248. <https://doi.org/10.1785/bssa0630010227>
- Oliver, J., & Ewing, M. (1957). Higher modes of continental Rayleigh waves. *Bulletin of the Seismological Society of America*, 47(3), 187–204.
- Page, B. M. (1981). The southern coast ranges. In W. G. Ernst (Ed.), *The geotectonic development of California* (pp. 329–417). Prentice-Hall.
- Phillips, W. S., & Aki, K. (1986). Site amplification of coda waves from local earthquakes in Central California. *Bulletin of the Seismological Society of America*, 76, 627–648.
- Phillips, W. S., & Stead, R. J. (2008). Attenuation of Lg in the western US using the USArray. *Geophysical Research Letters*, 35, L07307. <https://doi.org/10.1029/2007gl032926>
- Pikser, J. E., Forsyth, D. W., & Hirth, G. (2012). Along-strike translation of a fossil slab. *Earth and Planetary Science Letters*, 331, 315–321. <https://doi.org/10.1016/j.epsl.2012.03.027>
- Poland, J. F., & Evenson, R. E. (1966). Hydrogeology and land subsidence, great Central Valley, California. In E. H. Bailey (Ed.), *Geology of northern California: California division of mines and geology bulletin 190* (pp. 239–247). California Division of Mines and Geology.
- Ranasinghe, N. R., Gallegos, A., Hearn, T., Ni, J., & Sandvol, E. (2018). Frequency-dependent Lg attenuation in Northeast China and its implications. *Geophysical Journal International*, 212, 2131–2142. <https://doi.org/10.1093/gji/ggx522>
- Ranasinghe, N. R., Gallegos, A. C., Trujillo, A. R., Blanchette, A. R., Sandvol, E. A., Ni, J., et al. (2015). Lg attenuation in northeast China using NECESSArray data. *Geophysical Journal International*, 200(1), 67–76. <https://doi.org/10.1093/gji/ggu375>

- Rogers, A. M., Tinsley, J. C., Hays, W. W., & King, K. W. (1979). Evaluation of the relation between near-surface geologic units and ground response in the vicinity of Long Beach, California. *Bulletin of the Seismological Society of America*, 69, 1603–1622. <https://doi.org/10.1785/bssa0690051603>
- Schutt, D. L., Lowry, A. R., & Buehler, J. S. (2018). Moho temperature and mobility of lower crust in the western United States. *Geology*, 46, 219–222. <https://doi.org/10.1130/g39507.1>
- Shen, W., Ritzwoller, M. H., & Schulte-Pelkum, V. (2013). A 3-D model of the crust and uppermost mantle beneath the Central and Western US by joint inversion of receiver functions and surface wave dispersion. *Journal of Geophysical Research: Solid Earth*, 118, 262–276. <https://doi.org/10.1029/2012jb009602>
- Singh, S., & Herrmann, R. B. (1983). Regionalization of crustal coda Q in the continental United States. *Journal of Geophysical Research*, 88, 527–538. <https://doi.org/10.1029/jb088ib01p00527>
- Su, F., Aki, K., Teng, T., Zeng, Y., Koyanagi, S., & Mayeda, K. (1992). The relation between site amplification factor and surficial geology in central California. *Bulletin of the Seismological Society of America*, 82, 580–602.
- Tsai, Y. B., & Aki, K. (1969). Simultaneous determination of the seismic moment and attenuation of seismic surface waves. *Bulletin of the Seismological Society of America*, 59, 275–287. <https://doi.org/10.1785/bssa0590010275>
- Unsworth, M. J., & Bedrosian, P. (2004). Electrical Resistivity structure at the SAFOD site from magnetotelluric exploration. *Geophysical Research Letters*, 31, L12S05. <https://doi.org/10.1029/2003gl019405>
- Wang, Y., Forsyth, D. W., Rau, C. J., Carriero, N., Schmandt, B., Gaherty, J. B., & Savage, B. (2013). Fossil slabs attached to unsubducted fragments of the Farallon plate. *Proceedings of the National Academy of Sciences*, 110, 5342–5346. <https://doi.org/10.1073/pnas.1214880110>
- Wei, Z., Kennett, B. L., & Zhao, L. F. (2017). Lg-wave attenuation in the Australian crust. *Tectonophysics*, 717, 413–424. <https://doi.org/10.1016/j.tecto.2017.08.022>
- Xie, J., Gok, R., Ni, J., & Aoki, Y. (2004). Lateral variations of crustal seismic attenuation along the INDEPTH profiles in Tibet from Lg Q inversion. *Journal of Geophysical Research*, 109, B10308. <https://doi.org/10.1029/2004jb002988>
- Xie, J., & Mitchell, B. J. (1990). A back-projection method for imaging large-scale lateral variations of Lg coda Q with application to continental Africa. *Geophysical Journal International*, 100, 161–181. <https://doi.org/10.1111/j.1365-246x.1990.tb02477.x>
- Xie, J., & Mitchell, B. J. (1990). Attenuation of multiphase surface waves in the Basin and Range province, part I: Lg and Lg coda. *Geophysical Journal International*, 102, 121–137. <https://doi.org/10.1111/j.1365-246x.1990.tb00535.x>
- Yang, X. (2002). A numerical investigation of Lg geometrical spreading. *Bulletin of the Seismological Society of America*, 92, 3067–3079. <https://doi.org/10.1785/0120020046>
- Yassminh, R., Gallegos, A., Sandvol, E., & Ni, J. (2019). Investigation of the regional site response in the Central and Eastern United States. Investigation of the regional site response in the Central and Eastern United States. *Bulletin of the Seismological Society of America*, 109, 1005–1024. <https://doi.org/10.1785/0120180230>
- Zandt, G., Gilbert, H., Owens, T. J., Ducea, M., Saleeby, J., & Jones, C. H. (2004). Active foundering of a continental arc root beneath the southern Sierra Nevada in California. *Nature*, 431, 41–46. <https://doi.org/10.1038/nature02847>
- Zhang, H., & Thurber, C. (2005). Adaptive mesh seismic tomography based on tetrahedral and Voronoi diagrams: Application to Parkfield, California. *Journal of Geophysical Research*, 110, B04303. <https://doi.org/10.1029/2004jb003186>
- Zhao, L. F., & Mousavi, S. M. (2018). Lateral variation of crustal Lg attenuation in eastern North America. *Scientific Reports*, 8, 1–16. <https://doi.org/10.1038/s41598-018-25649-5>
- Zhao, L. F., Xie, X. B., He, J. K., Tian, X., & Yao, Z. X. (2013). Crustal flow pattern beneath the Tibetan Plateau constrained by regional Lg-wave Q tomography. *Earth and Planetary Science Letters*, 383, 113–122. <https://doi.org/10.1016/j.epsl.2013.09.038>
- Zhao, L. F., Xie, X. B., Wang, W. M., & Yao, Z. X. (2008). Regional seismic characteristics of the 9 October 2006 North Korean nuclear test. *Bulletin of the Seismological Society of America*, 98, 2571–2589. <https://doi.org/10.1785/0120080128>
- Zhao, L. F., Xie, X. B., Wang, W. M., Zhang, J. H., & Yao, Z. X. (2010). Seismic Lg-wave Q tomography in and around Northeast China. *Journal of Geophysical Research*, 115. <https://doi.org/10.1029/2009jb007157>
- Zhao, L. F., Xie, X. B., Wang, W. M., Zhang, J. H., & Yao, Z. X. (2013). Crustal Lg attenuation within the North China Craton and its surrounding regions. *Geophysical Journal International*, 195, 513–531. <https://doi.org/10.1093/gji/ggt235>

Reference From the Supporting Information

- Chen, Y., & Xie, J. (2017). Resolution, uncertainty and data predictability of tomographic Lg attenuation models—Application to southeastern China. *Geophysical Journal International*, 210, 166–183.